RSC Advances

PAPER

View Article Online
View Journal | View Issue

Cite this: *RSC Adv.*, 2020, **10**, 7541

Multidimensional structure of $CoNi_2S_4$ materials: structural regulation promoted electrochemical performance in a supercapacitor†

Yue Han, [a] Shishuai Sun,*[a] Wen Cui*[b] and Jiachun Deng[a]

Multidimensional architectures of $CoNi_2S_4$ electrode materials are rationally designed by engineering the surface structure toward that of high-performance supercapacitors. The fabrication of a special morphology is highly dependent on the synergistic effect between the guidance of Co–Ni precursor arrays and a subsequent sulfidation process. The unparalleled $CoNi_2S_4$ electrode materials (NS-3) deliver a significantly enhanced specific capacitance (3784.6 F g^{-1} at 3 A g^{-1}), accompanied by an extraordinary rate capability (2932.3 F g^{-1} at 20 A g^{-1}) and excellent cycling life. The outstanding supercapacitor performance stated above stems from the advantages of a multidimensional structure generated by crosslinking 2D microsheets/1D nanowires/2D ultrathin nanosheets; this structure supplies additional efficient active sites and a large contact area at the electrode–electrolyte interface, providing faster transport kinetics for electrons and ions. For practical applications, asymmetric devices based on an NS-3 positive electrode and active carbon negative electrode exhibit a high energy density of 38.5 W h kg^{-1} accompanied by a power density of 374.9 W kg^{-1} (22 W h kg^{-1} at 7615.4 W kg^{-1}). The above results indicate that the design of multidimensional Co–Ni–S materials is an effective strategy to achieve a high-performance supercapacitor.

Received 29th December 2019
Accepted 10th February 2020

DOI: 10.1039/c9ra10961g

rsc.li/rsc-advances

1. Introduction

The development of safe and environmentally friendly green energy technologies to address the current energy and environmental crisis is of great significance, and there are promising prospects for developing sustainable energy for the economy and society.[1–6] As a promising energy storage device, supercapacitors (SCs) are receiving considerable attention due to their low cost, high power density, and fast charge and discharge.[7–9] Based on the energy storage mechanism of SCs, designing an advanced faradaic pseudocapacitor material as an electrode is an effective strategy to prepare desired supercapacitors owing to the higher energy storage capacity of the material in comparison with those of various materials used in double-layer energy storage mechanisms.[10,11] Nevertheless, a low electron conductivity and short ion diffusion length of the active materials drastically limit their capacitance behavior.[12–14] To solve bottleneck issues, a key problem is to construct an ideal electrode material with unique structural and component characteristics for exposing an abundance of active sites on the surface and improving the charge and ion transport mechanism.[15,16]

The design of low-dimensional nanostructure materials can evidently boost the electrochemical activity of electrodes by offering fast redox reaction kinetics, highly accessible active sites and improving electronic/ionic conductivity.[17] Regrettably, the practical utilization efficiency of the electrode material and the diffusion distance of electrolyte are low due to an aggregation of low-dimensional nanomaterial into a bulk or into bundled stacks.[18–20] In comparison, fabricating a multidimensional structure with a high-curvature surface, an abundance of open channels, and advantageous low-dimensional structural units is an effective strategy to maximize the utilization efficiency of electrode materials.[21–23] In addition, binary metal sulfide has attracted much research due to its prominent characteristics, such as higher electrical conductivity and higher theoretical specific capacity than those of a unitary metal sulfide. Therefore, researchers combine the intrinsic advantages of a multidimensional structure and the unique superiority of a binary metal sulfide to improve the electrochemical performance of materials, especially three-dimensional (3D) hierarchical cobalt nickel sulfide (Co–Ni–S) materials.[24–28] For example, a specific capacitance of 1102.22 F g^{-1} can be achieved when 3D rambutan-like hierarchical $CoNi_2S_4$ is used as an electrode at a current density of 1 A g^{-1}.[29] 3D-nanostructured $CoNi_2S_4/Co_8S_9$ nanocomposites have a specific capacitance of 1183.3 F g^{-1} at a current density of 2 A g^{-1}.[30] The 3D $NiCo_2S_4$/

[a]College of Science, Tianjin University of Technology, Tianjin 300384, China. E-mail: sssdashuai@email.tjut.edu.cn

[b]College of Physics and Materials Science, Tianjin Normal University, Tianjin, 300387, China. E-mail: cuiwen2005xj@126.com

† Electronic supplementary information (ESI) available. See DOI: 10.1039/c9ra10961g

$Co_xNi_{(3-x)}S_2$ core/shell nanoarray structure reveals a high specific capacitance of 1950 F g^{-1} at 10 mA cm^{-1}.[31] It is unfortunate that the above strategies still do not lead to a satisfactory capacity for practical applications of Co–Ni–S materials. Inspired by previous reports, there is still a need for in-depth research on designing additional structures for Co–Ni–S materials to fulfill a need for high electrochemical performance.[32–34]

In the present work, we attempt to increase the electrochemical performance of $CoNi_2S_4$ by tuning its morphology and microstructure. The four types of $CoNi_2S_4$ morphology are fabricated by a two-step synthesis strategy utilizing hydrothermal and sulfidation processes. The formation mechanism of the multidimensional $CoNi_2S_4$ structure is discussed by a systematic investigation of the growth and sulfidation process of the Co–Ni precursor that results in the regulation of the microstructure. Among the four types of $CoNi_2S_4$ materials, the rational design of NS-3 as a free binder electrode exhibits optimal electrochemical performance compared with that of other samples (3784.6 F g^{-1} at 3 A g^{-1}). Such excellent electrochemical performance of NS-3 originates from the merit of multidimensional structural arrays directly grown array on Ni foam (NF) consisting of crosslinked two-dimensional (2D) microsheets/one-dimensional (1D) nanowires/2D ultrathin nanosheets, which not only provides a wealth of porous channels and active sites for faradaic reactions but also possesses better transport performance of ions and electrons than other samples possess. Furthermore, the asymmetric supercapacitors ASC device of the NS-3 electrode coupled with active carbon (AC) displays a high energy density (38.46 W h kg^{-1} at a power density of 374.9 W kg^{-1}, 22 W h kg^{-1} at a power density of 7615.4 W kg^{-1}).

2. Experimental

2.1 Material synthesis

The reaction chemicals reagents are cobalt nitrate hexahydrate ($Co(No_3)_2 \cdot 6H_2O$), nickel nitrate hexahydrate ($Ni(NO_3)_2 \cdot 6H_2O$), ammonium fluoride (NH_4F), urea (CON_2H_4), and sodium sulfide ($Na_2S \cdot 9H_2O$), which are the analytical grade. The surface of NF (3 × 1 × 0.1 cm) is cleaned by the 3 M hydrochloric acid, acetone, ultrapure water and analytically ethanol in turn for 30 min. Subsequently, the NF are dried at 60 °C in an vacuum drying oven. The mass of the treated nickel foam was denoted as M_1.

Preparation of the Co–Ni precursor. $Co(No_3)_2 \cdot 6H_2O$ (1 mmol), $Ni(NO_3)_2 \cdot 6H_2O$ (0.5 mmol), different NH_4F concentrations (0, 1, 2, 3, 4, 6 and 9 mmol) and CON_2H_4 (6 mmol) are mixed in 40 mL of deionized water by magnetic stirring. Then, the mixed solution is transferred into a 50 mL Teflon stainless steel autoclave, and a piece of cleaned NF is slowly immersed. The sealed autoclave is placed in a drying oven for a drying time of 8 h at 120 °C. After the experiment is finished, the sealed autoclave is cooled to room temperature. The obtained Co–Ni precursor is cleaned with ultrapure water and absolute ethanol to remove any residual chemical reagent adsorbed on the surface of the precursor and then it is dried at 60 °C in a vacuum oven. The Co–Ni precursor samples are marked as NP-0, NP-1, NP-2, NP-3, NP-4, NP-6, NP-9 according to the amount of NH_4F used. The mass loading of precursor on nickel foam is denoted as M_2. The mass loading of NP sample on each square centimeter of nickel foam is calculated by $(M_2 - M_1)/3$.

Preparation of the Co–Ni–S. The prepared solution, including 40 mL of ultrapure water and 0.2 mmol of sodium sulfide ($Na_2S \cdot 9H_2O$), is transferred into 50 mL Teflon-lined autoclave. Then, the synthesized Co–Ni precursor is immersed. The sealed autoclave is placed in a drying oven for a drying time of 4 h at 120 °C. The obtained Co–Ni–S materials are cleaned with ultrapure water and absolute ethanol to remove the residual chemical reagent adsorbed on the surface of the material and then the material is dried at 60 °C in a vacuum oven. The final samples are marked as NS-0, NS-1, NS-2, NS-3, NS-4, NS-6, and NS-9 according to the amount of NH_4F used. The mass loading of final vulcanized sample on nickel foam is denoted as M_3. The mass loading of NS samples on each square centimeter of nickel foam is calculated by $(M_3 - M_1)/3$. Finally, the calculated mass loading of NS-3 is 1.36 mg cm^{-2}.

2.2. Material characterization

The crystal structure and chemical compositions of the prepared Co–Ni–S electrode materials are analyzed by X-ray diffraction (XRD, Rigaku SmartLab D/max 2500 PC) operated at 40 kV using Cu Kα radiation from 10 to 80 angles at a scanning rate of 6° min^{-1}. The element distribution and chemical state of the electrode materials are tested by the X-ray electron diffractometer (XPS, ESCALAB 250Xi). Observation and analysis of surface micro-nano structures are processed by field-emission scanning electron microscopy (SEM, Quanta FEG 250) operated at 8 kV. Transmission electron microscope (TEM, JEM 2010FEF operated at 1200 kV) is also run to further observe the microstructure of the prepared material.

2.3. Electrochemical performance measurements

The electrochemical tests are performed by an AUTOLAB87348 electrochemical instrument. The performance of the obtained samples (1 × 1 cm) directly used as the working electrode is first performed in a three-electrode system with a 2 M KOH aqueous solution as the electrolyte. The reference and counter electrodes are Hg/HgO and Pt foil, respectively. Testing methods include cyclic voltammetry (CV), galvanostatic charging/discharging (GCD) and electrochemical impedance spectroscopy (EIS). The specific capacity C (F g^{-1}) can be calculated using eqn (1):

$$C = I\Delta t/m\Delta V \quad (1)$$

where I corresponds to discharge current (A g^{-1}), Δt represents the discharge time (s), m is the loading amount of electroactive materials (mg) and ΔV refers to the working voltage (V) range.

In a two-electrode system, the obtained Co–Ni–S nanostructure material (NS-3, 1.36 mg cm^{-2}) is directly used as the positive electrode. A slurry of active carbon (AC), carbon black, and polytetrafluoroethylene (PTEE) in a weight ratio of 80 : 10 : 10 is coated on an NF to fabricate the negative

electrode. The prepared asymmetric supercapacitors (ASC) include a positive electrode of NS-3, a negative electrode of AC, a one-piece separator of cellulose paper, and an electrolyte of 2 M KOH. During the assembly of the ASC, the charge balance theory ($q^+ = q^-$) determines the mass loading ratio of the two electrodes as follows:

$$\frac{m_+}{m_-} = \frac{C_-\Delta V_-}{C_+\Delta V_+} \quad (2)$$

The energy density E (W h kg^{-1}) of ASCs is related to the power density P (W kg^{-1}) and can be defined by the following eqn (3) and (4):

$$E = \frac{C_A \times \Delta V_A{}^2}{2 \times 3.6} \quad (3)$$

$$P = \frac{3600 \times E}{\Delta t} \quad (4)$$

where C_A, ΔV_A, and Δt represent the specific capacitance, voltage range and discharge time of the ACSs, respectively.

3. Results and discussion

Fig. 1 clearly shows the synthesis process of the multidimensional Co–Ni–S structure by a two-step growth method. In the first step, hierarchical Co–Ni precursor arrays are vertically formed on NF *via* an *in situ* hydrothermal reaction between Co^{2+} and Ni^{2+} ions, and hydrolysis products released from CoN_2H_4 and NH_4F. The precursor can be described as $NiCo_2(CO_3)_{1.5}(OH)_3$, which is confirmed by XRD (Fig. S1†).[35] Subsequently, a hybrid-dimensional $CoNi_2S_4$ structure can be obtained from an anion exchange reaction between S^{2-} derived from Na_2S solution and anions (OH^- and $CO_3{}^{2-}$) derived from the Co–Ni precursor, which is also confirmed by XRD results (Fig. S2†). Interestingly, four different morphologies of Co–Ni precursor can be constructed during the whole experimental process with different amounts of NH_4F (step I). After the second step of hydrothermal vulcanization, the different nanostructures of the Co–Ni–S array are well fabricated by the induction of Co–Ni precursor, as shown in Fig. 1b–e (step II). When no NH_4F is added in the step I, the final obtained Co–Ni–S nanostructure (NS-0) from step II reveals that a large number of 1D nanowire arrays accompany the formation of 2D nanosheet clusters at the tip of the nanowires (Fig. 1b). When 1 mmol of NH_4F is added, the images of obtained NS-1 show that 1D nanowires are obviously wrapped by 2D ultrathin nanosheets (Fig. 1c). When the amount of NH_4F added increases to 3 mmol, the structure of NS-3 is composed of 2D microsheets (length of ≈5 μm) and 1D nanowires (diameter of ≈50 nm) decorated by 2D ultrathin nanosheets uniformly covering the Ni foam surface, which forms an architecture with a large area connected with a highly porous structure (Fig. 1d). 1D hollow nanotube arrays of NS-6 are finally formed when the amount of NH_4F rises to 6 mmol (Fig. 1e).

Information on the structure and composition of the Co–Ni–S samples are verified by TEM analysis (Fig. 2). The typical TEM images of NS-0 show that the tip of 1D nanowires are the cluster

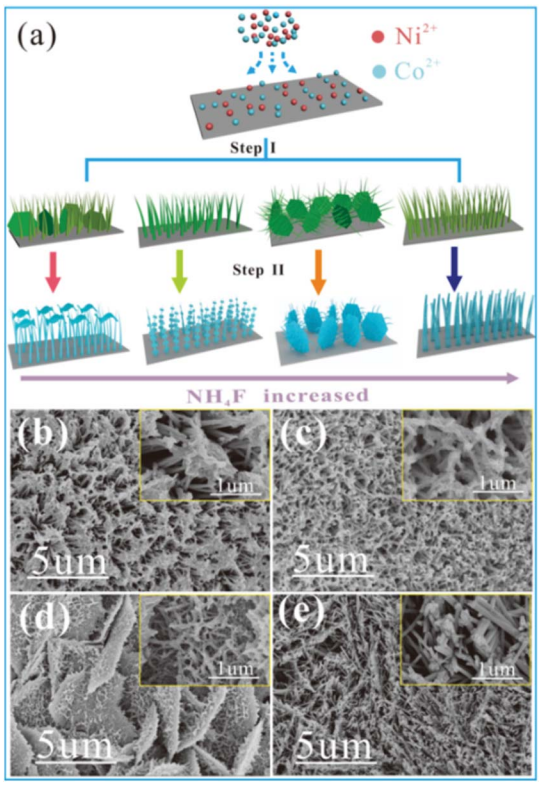

Fig. 1 (a) Schematic illustration of the Co–Ni–S multidimensional structural morphology synthesized by a hydrothermal (step I) and sulfidation (step II) process. SEM images of the NS-0 sample (b); NS-1 sample (c); NS-3 sample (d) and NS-6 sample (e).

of ultrathin nanometer sheet (Fig. 2a–c). However, the overall of 1D nanowires of NS-1 and NS-3 are covered by ultrathin or silk-like 2D nanosheets (Fig. 2d–i), which is consistent with the SEM

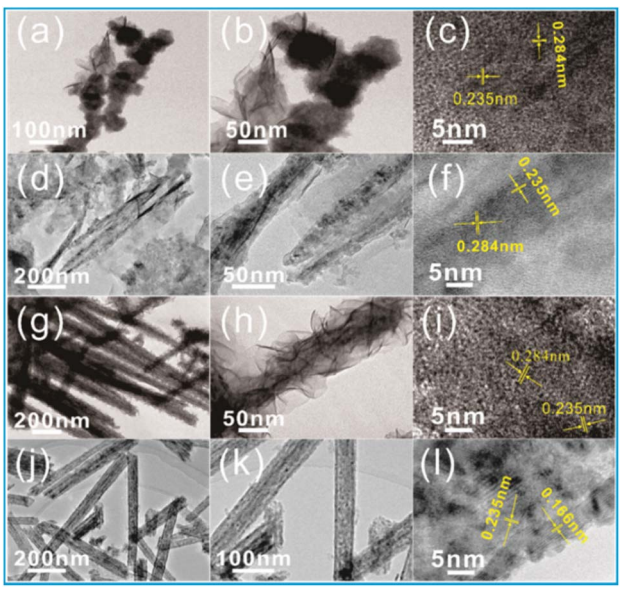

Fig. 2 HRTEM and SRED images of the NS-0 sample (a–c); NS-1 sample (d–f); NS-3 sample (g–i); and NS-6 sample (j–l).

results. When NH_4F is used in large quantities, TEM images of NS-6 show the clearly 1D nanotubes structure with the average diameter (thickness) of 100 nm (12 nm) consisting of a large number of 0D nanoparticles (Fig. 2g–i). The HR-TEM image displays the visible lattice fringe spacing of 0.166 nm, 0.284 nm and 0.235 nm, corresponding to the distance of (440), (311) and (400) planes of the $CoNi_2S_4$, which is consistent with the results of XRD. Our results indicate that although the addition ratio of moles of cobalt nitrate to nickel nitrate is 2 : 1 in the reaction solution, the ratio of Co : Ni in the obtained samples is 1 : 2 due to its special reaction conditions. The SEM and TEM results also indicate that the structure of synthesized samples belong to multi-dimensional mixed.

It is worth mentioning that the special morphology of NS-3 composing the crosslinked 2D microsheets/1D nanowires/2D ultrathin nanosheets is different from that of previous reports. An EDS and XPS analysis are conducted to determine the elemental composition and binding energy information of the NS-3 samples (Fig. 3). Fig. 3a–e reveals the uniform distribution of Co, Ni, and S elements in the structure, which can also be detected by the XPS peaks (Fig. 3f). The peaks at 778.8 and 794.4 eV imply the existence of Co^{2+}, while the peaks at 781.3 and 796.8 eV match with Co^{3+} in the Co 2p spectrum with two satellites (denoted as "sat") (Fig. 3g).[36] The Ni 2p peaks are positioned at 853.1 and 873.5 eV indexing to the Ni^{2+} and at 856.8 and 874.6 eV corresponding to Ni^{3+} (Fig. 3h). Fig. 3i shows

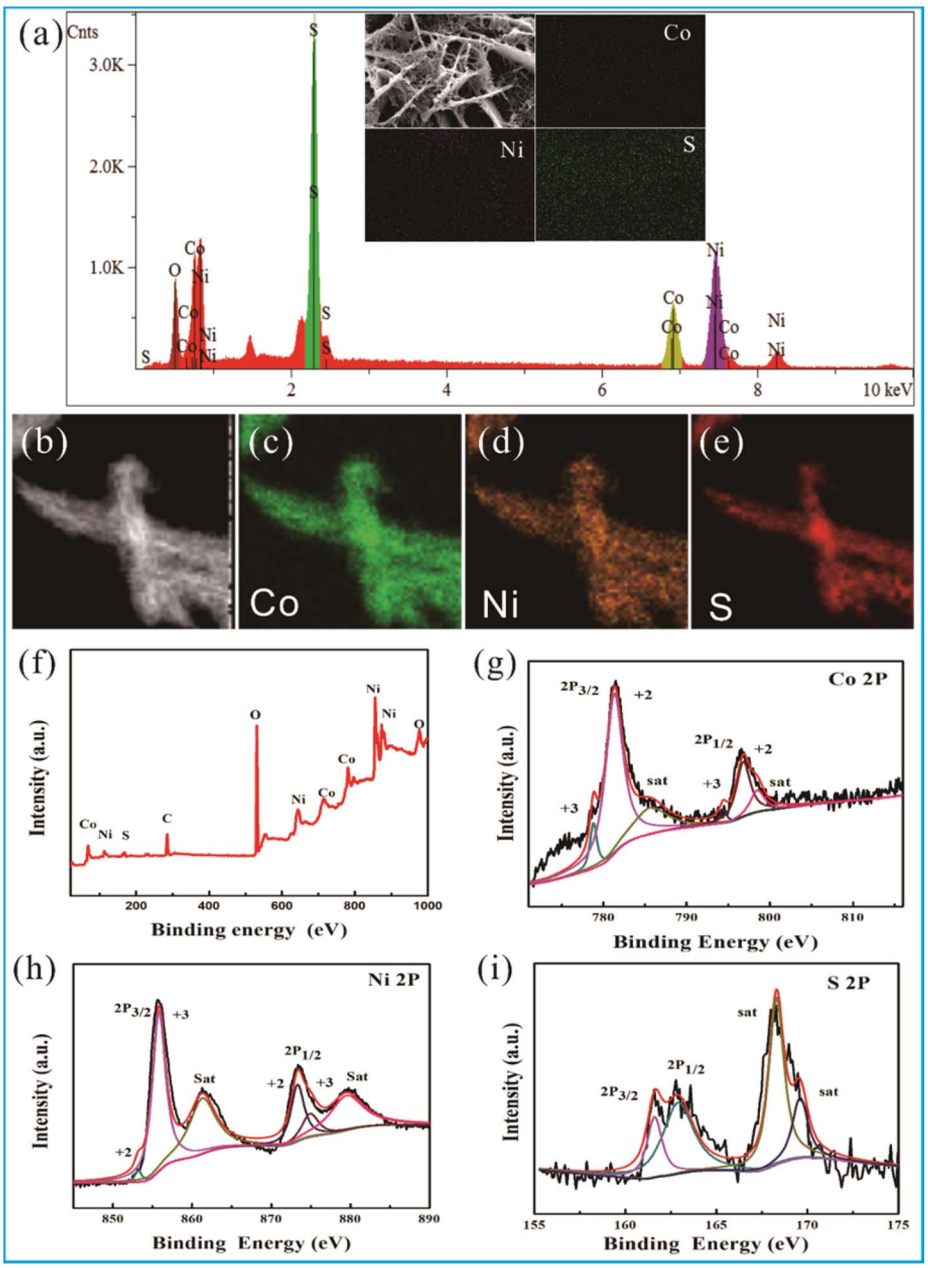

Fig. 3 (a) EDS analysis of the NS-3 sample. (b–e) Overlapped elemental mapping image of NS-3 and the corresponding elemental distribution mapping images of the NS-3 sample. XPS spectra of the NS-3 sample: (f) survey, (g) Co 2p, (h) Ni 2p, and (i) S 2p.

the presence of S^{2-} related to the peaks of 162.9 and 161.6 eV, which correspond to S $2p^{1/2}$ and S $2p^{3/2}$, respectively. Furthermore, peaks at 168.1 and 169.2 eV are observed due to the presence of sulfur vacancies from the metal–S site at the surface, which generates additional active sites and enhances the intrinsic conductivity of the material.[29,36,37]

To clarify the evolution mechanism of the multidimensional morphology, especially for NS-3, we first study the evolution process of the Co–Ni precursor morphology affected by the reaction time (Fig. S3†). At an early stage of growth (0.5 h), the 2D microsheets uniformly and vertically grown on the Ni foam are dominant (Fig. S3a and b†). With increasing reaction time to 1 h, 1D nanowires gradually appear on the edge of the 2D microsheets (Fig. S3c and d†). When the reaction time is prolonged to 8 h, the length and diameter of the 1D nanowires with a high density are further increased. Interestingly, these 1D nanowires not only grow on the edges of the 2D microsheets but also penetrate their surface, forming 3D structures (Fig. S3e and f†). The hierarchical Co–Ni precursor finally evolve into 1D nanowire arrays with lengths of several micrometers after a reaction time of 12 h (Fig. S3g and h†). Experimental results show that a short reaction time will help the formation of 2D microsheets, and a long reaction time will be favorable to form the 1D nanowires. With the change of reaction time, the evolved morphology of the Co–Ni precursor (Fig. S3†) are mainly related to NH_4F in the reaction of step I. The chemical reactions involved in the preparation of Co–Ni precursors are as follows:[38,39]

$$Ni^{2+}(Co^{2+}) + xF^- \rightarrow [Ni(Co)F_x]^{(x-2)-} \quad (5)$$

$$Co(NH_2)_2 + H_2O \rightarrow 2NH_3 + CO_2 \quad (6)$$

$$CO_2 + H_2O \rightarrow {CO_3}^{2-} + H^+ \quad (7)$$

$$NH_3 \cdot H_2O \rightarrow {NH_4}^+ + OH^- \quad (8)$$

$$[Ni(Co)F_x]^{(x-2)-} + (1 - 0.5y){CO_3}^{2-} + yOH^- + nH_2O \rightarrow Ni(Co)(OH)_y({CO_3}^{2-})(1 - 0.5)y \cdot nH_2O + xF^- \quad (9)$$

At the beginning, the Ni^{2+} and Co^{2+} metal ions first coordinate with the F^- released from the NH_4F to form the $[Ni(Co)F_x]^{(x-2)-}$ in the mixed solution before heating. As the temperature of reaction chamber increases, the $CO(NH_2)_2$ can hydrolyze to OH^- and ${CO_3}^{2-}$, which can reacts with metal ions slowly released form the $[Ni(Co)F_x]^{(x-2)-}$ to form the Co–Ni precursor.[39,40] At the same time, the presence of F^- in the solution generated form the hydrolysis of NH_4F can corrode the Co–Ni precursor. In the early stage of the reaction, the hydrolysis of NH_4F generates the low concentration of F^- in the system, which is benefit to the formation of 2D microsheets with high specific surface area and low surface energy.[41] However, the hydrolysis rate and strength of NH_4F are significantly enhanced with the increasing of reaction time, leading to a sharp decrease of PH value. Meanwhile, the etching of Co–Ni precursor by high concentration of F^- is further deepened, which drives the growing of 1D nanowires preferentially at the rough (etch) edges of 2D microsheets. With further etching of 2D microsheets and growth of 1D nanowires, 2D microsheets fully evolve into 1D nanowires with high density (Fig. S3g and h†). To further prove the correct of our analysis, we also study the evolution process of the Co–Ni precursor morphology affected by the different amounts of NH_4F under the same reaction time (Fig. S4†). The results of growth process of the Co–Ni precursor affected by the concentration of NH_4F indicates that the stability of morphology is in the order of nanowires > microsheets > nanosheets in the presence of a high concentration of NH_4F. When the reaction time is the same, the higher concentration of NH_4F will result in the deeper degree of etching of the generated Co–Ni precursor, helping the formation of nanowires, which efficiently support our above analysis.

The sulfidation process is also responsible for the formation of the multidimensional structures. The Ni–Co precursor arrays are successfully converted to $CoNi_2S_4$ arrays with a hybrid-dimensional structure based on the anion exchange reaction in the presence of aqueous $Na_2S \cdot 9H_2O$. It should be noted that the morphology after the sulfidation process is changed compared with that of the Ni–Co precursor. Obviously, the 1D nanowires of NS-3 are covered by 2D ultrathin nanosheets, while the 1D nanowires of NS-6 transform into 1D nanotubes. In fact, the precursor of 1D nanowires of NS-6 are highly etched by the large concentration of F^-, creating a large point defect, which will accelerate the efficiency of sulfidation reactions and lead to the growth of 1D nanotubes.[42] This can be certified by the results of the TEM images of NS-9, showing that the characteristics of the 1D nanotube structure that consist of 0D nanoparticles are more distinct (Fig. S5†). Therefore, there is a synergistic effect between the guidance of the Co–Ni precursor arrays and the sulfidation process when forming the multidimensional morphology of the $CoNi_2S_4$ arrays.

To further explore the performances of the electrode materials in relation to their structure, a series of tests are first run in a three-electrode system as described by the section of electrochemical performance measurements. Remarkably, the NS-3 electrode has the largest integral area and longest discharge time than those of the other electrodes in the CV and GCD curves, as shown in Fig. 4a and b; thus, it possesses the largest specific capacity. A more detailed performance of the NS-3 electrode is further investigated in Fig. 4c. With an increase in the scanning rate, the peak position of the cathode moves toward the lower potential attributed to the polarization effect. The related peaks of the redox reaction match the following reaction equations:[43,44]

$$CoS + OH^- \leftrightarrow CoSOH + e^- \quad (10)$$

$$CoSOH + OH^- \leftrightarrow CoSO + H_2O + e^- \quad (11)$$

$$NiS + OH^- \leftrightarrow NiSOH + e^- \quad (12)$$

In the GCD test, the symmetric curves of charge–discharge time with a distinct plateau prove the excellent reversibility of the faradaic reaction processes (Fig. 4d). The specific capacitance from the NS-3 GCD curves are determined to be 3784.6, 3510.8, 3399.5, 3131.5, and 2932.3 F g^{-1} at 3, 5, 8, 10, and 20 A g^{-1}, respectively, which are much higher than those of the

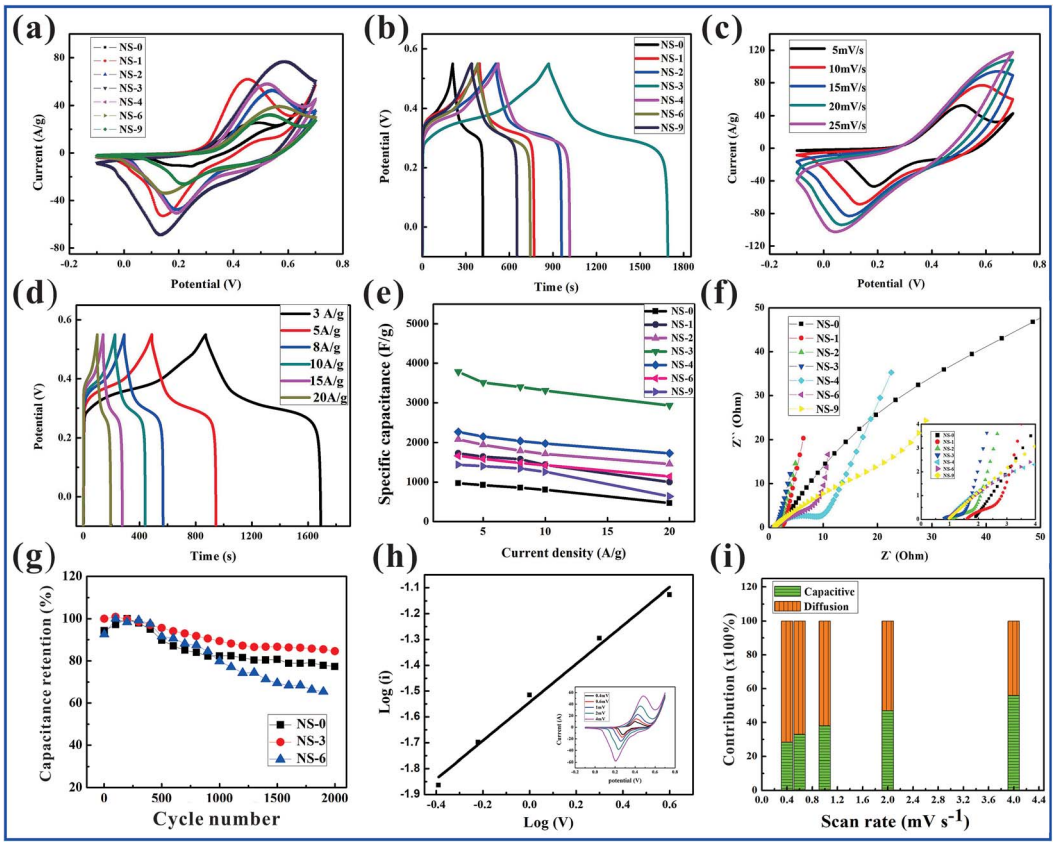

Fig. 4 (a and b) CV and GCD curves of NS-0–NS-9 under 10 mV s^{-1} and 3 A g^{-1}, respectively. (c and d) CV and GCD curves of the NS-3 electrode performed at different scan rates and current densities. (e) Comparison of the curves of the specific capacitance for NS-0–NS-9. (f) EIS of NS-0–NS-9. (g) Cycling life of NS-0, NS-3, and NS-6 measured at 20 mV s^{-1}. (h) Relationship between the current and scan rate of the NS-3 electrode material (the inset image are the CV curves from 0.4 to 4 mV s^{-1}). (i) Analysis of the surface capacitance contribution toward the whole capacitance of the NS-3 electrode.

other comparative NS samples and those of the Co–Ni precursors (Fig. 4e and S6a, b,† respectively).

EIS was performed to evaluate the electrical conductivity of the electrode materials (Fig. 4f). The tests show that the equivalent series resistance values (R_s) determined by the intercept of the real axis and the charge-transfer resistance (R_{ct}) calculated by the diameter of the semicircle of NS-3 are 0.754 Ω and 0.919 Ω, respectively; these values are much smaller than those of the other samples and the Co–Ni precursors (Fig. S6c and d†), suggesting NS-3 has a better electrical conductivity.[33,45] Furthermore, the slope of the line for the NS-3 electrode is almost perpendicular to the real axis in the low-frequency region suggesting the outstanding mobility kinetics of the ions. Fig. 4g shows an 84.6% capacitance retention for the $CoNi_2S_4$ electrode (NS-3) even after 2000 cycles, which is superior to the cyclic stability of NS-0 (77.3%) and NS-6 (65.4%).

The storage mechanism of NS-3 in the redox reaction is also studied by CV measurements employing low scan rates (0.4 to 4.0 mV s^{-1}) (Fig. 4h). The current (i) in relation to the scan rate (v) can be defined by the equation:[46,47]

$$i = av^b \tag{13}$$

Generally, the value of b is confined at 0.5 to 1, which depends on the slope relationship between $\log(i)$ and $\log(v)$. A diffusion-controlled process corresponds to a value of 0.5, while a capacitance-dominated process corresponds to a b value of 1.0. In this study, the calculated b value for the anodic peaks of NS-3 is 0.74. Hence, NS-3 exhibits battery-type capacitor behavior *via* diffusion processes. In fact, we can analyze the surface capacitance contribution toward the whole capacitance in depth according to the following equation:

$$i(V) = k_1v + k_2v^{1/2} \tag{14}$$

where $i(V)$ represents the total current, k_1v refers to the capacitance effect and $k_2v^{1/2}$ represents the diffusion-controlled process. By plotting $i(V)/v$ *vs.* $v^{1/2}$ to calculate the k_1 and k_2 values, we can designate the NS-3 electrode contribution ratios toward the capacitance effect as being 28.40%, 33%, 38%, 47% and 56% at scan rates of 0.4, 0.6, 1, 2 and 4 mV s^{-1}, respectively. This result evidently indicates that the charge storage is mainly controlled by the diffusion process at a low scan rate, which is a typical faradaic characteristic of electrode material.

It is well known that the electrochemical performance of materials used as supercapacitor electrodes are highly

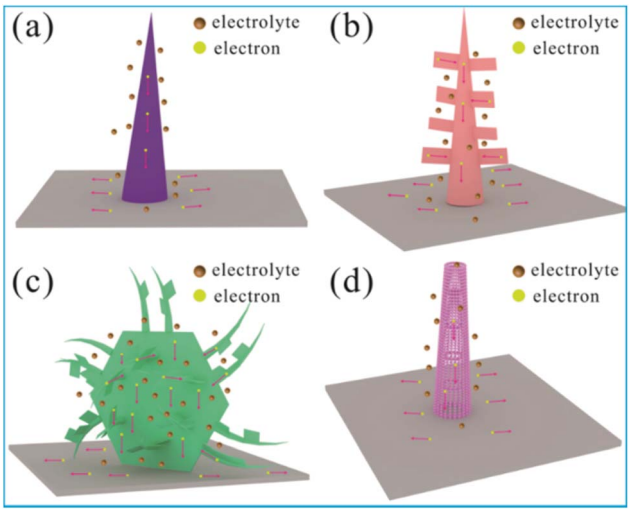

Fig. 5 Charge storage mechanism of the electrode based on the merits of each structure. (a) 1D nanowires; (b) 1D nanowires/2D nanosheets; (c) 2D microsheets/1D nanowires/2D nanosheets/; (d) 0D nanoparticles/1D nanocubes.

depended on their micro-nano structures, which have different surface active sites for redox reactions and the channel of electron and ion transport diffusion.[48–50] In fact, the results of SEM and HRTEM obviously show that the four samples have different multi-dimensional structures providing the different ion transport diffusion channel and electrochemically active sites, as shown in Fig. 5. In addition, EIS tests also show that there are different equivalent series resistance values and the charge-transfer resistance for the obtained four samples (Fig. 4f), implying the different electrical conductivity for the electron transfer. Although the phase composition of these four sulfide samples is the same, the charge storage mechanism of these four sulfide samples is different due to the characteristic of structure. As the typical materials, the unique multidimensional structures of NS-3 induce remarkable electrochemical performance increases as a result of the following features: (1) the units containing low-dimensional micro/nanostructures (1D nanowires, 2D ultrathin nanosheets and 2D microsheets) offer additional active sites for redox reactions due to a large surface area. (2) Multidimensional hybrid structures not only prevent the stacking of low-dimensional structures but also provide a large porous channel for accelerating ion transport

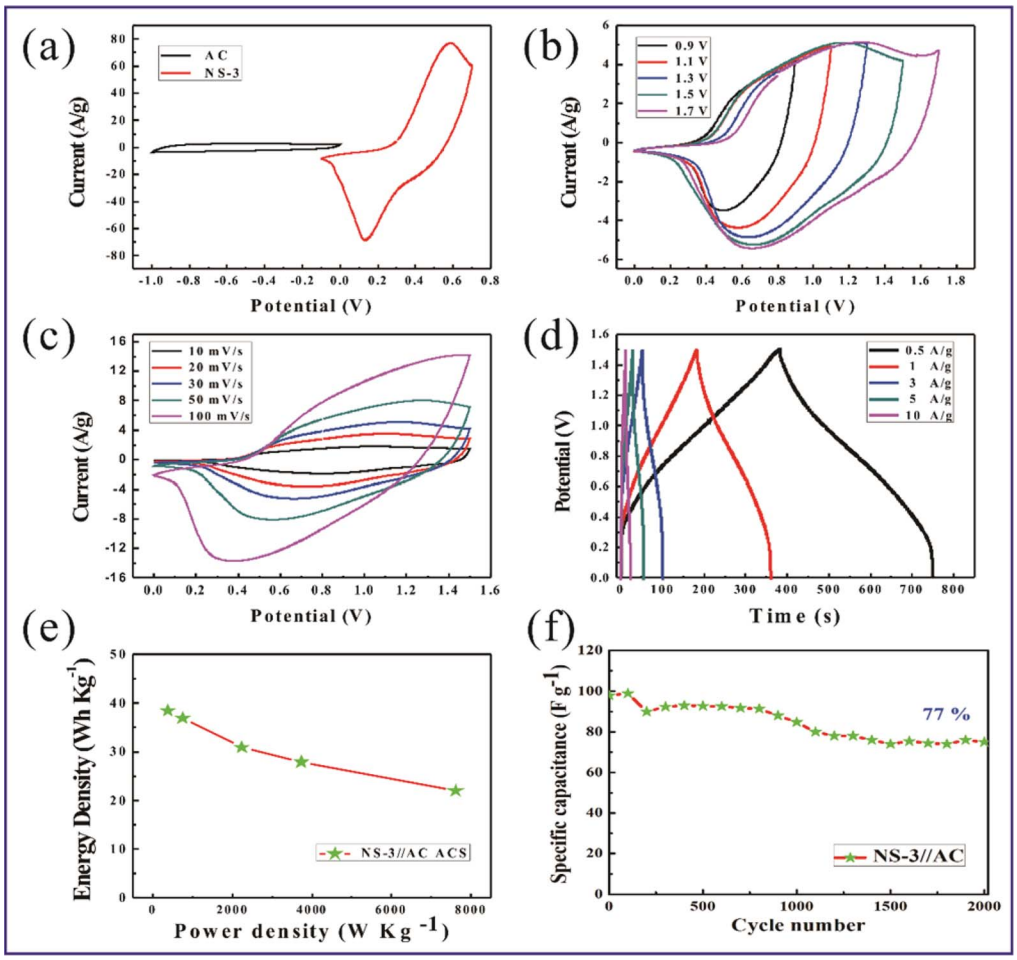

Fig. 6 (a) Comparison of the CV curves between NS-3 and AC electrodes at 30 mV s^{-1}. (b) CV curves of the NS-3//AC ASCs operated at different voltage ranges. (c) CV curves of the ASCs working at a scan speed of 10–100 mV s^{-1}. (d) GCD curves of ASCs run at current densities of 0.5–10 A g^{-1}. (e) Ragone plots of the ACS devices. (f) Stability test of the NS-3//AC device operated at 3 A g^{-1} over 2000 cycles.

diffusion and enhancing the probability of electrolyte contact with the surface of the electrode, especially in the presence of 2D microsheets. (3) The intrinsic conductivity of the electrode materials is enhanced after the sulfidation process, which was attributed to the generation of surface defect sites. (4) Multidimensional structures grown on conductive NF substrates without any additional polymer binder improve the binding force between the materials and substrates, further ensuring rapid electron transfer and cycling stability.

ASC devices are fabricated to test the application potential of the NS-3 positive electrode. The negative performance of the AC electrode used in the ASC devices is represented in Fig. S7† under a three-electrode test system. The comparison of CV curves in Fig. 6a shows that the stable working voltage range of the NS-3 and AC electrodes are −0.1–0.7 V and −1–0 V at a scan rate of 30 mV s^{-1}, respectively. To confirm the stable working voltage range of the ASC devices, the CV curves are run at different voltage ranges, as shown in Fig. 6b. It is obvious that the NS-3//AC supercapacitor can realize an operating voltage of 1.7 V without obvious polarization caused by an oxygen evolution reaction. In practice, a voltage range of 0–1.5 V provides the best stability of the device. The corresponding CV profiles of Fig. 6c at different scan rates reveal the synergistic effect between the faradaic and electrical double-layer capacitance for the ASC device. It is interesting to note that no severe deformation can be seen even under a high scan speed of 100 mV s^{-1} (Fig. 6c). The GCD measurements depict symmetric charge–discharge curves at each current density shown in Fig. 6d. The results of the CV and GCD analysis imply an excellent transport performance for ions and electrons and an excellent reversibility of the NS-3//AC ACSs. The calculated specific capacitance of devices based on the GCD curves is 123.07, 118.2, 99, 89.3 and 70.7 F g^{-1} corresponding with current densities of 0.5, 1, 3, 5 and 10 A g^{-1}, respectively. The plot of energy density with the change of power density is revealed in Fig. 6e. At a power density of 374.9 W kg^{-1} (7615.4 W kg^{-1}), the device delivers a high energy density of 38.5 W h kg^{-1} (22 W h kg^{-1}). For the measurements of cycling stability, the NS-3//AC ACS exhibits a retained capacitance of 77% compared with the initial capacitance after 2000 cycles at 3 A g^{-1} (Fig. 6f). In fact, there are many different aspects between the three-electrode cell and two-electrode cell resulting in the different performance, such as the applied voltage and charge transfer across the electrode, the mass of the active material and thickness of the electrodes.[51] Generally, the three-electrode cell yields higher value than those of the two-electrode cell, which is similar as our work that the ACS exhibits a lower cycling stability than three-electrode cell. Even so, our results indicate that the design of multidimensional Co–Ni–S materials is an effective strategy to achieve a high-performance supercapacitor.

4. Conclusions

In summary, different morphologies of Co–Ni–S materials with multidimensional structures are designed to improve the electrochemical performance of supercapacitors. There is a synergistic effect between the guidance of Co–Ni precursor arrays in relation to the amount of NH_4F and sulfidation process when forming the multidimensional morphology of $CoNi_2S_4$ arrays. Based on the advantages of a multidimensional structure composed of crosslinked 2D microsheets/1D nanowires/2D ultrathin nanosheets, an optimized NS-3 electrode exhibits an obviously enhanced specific capacity (3784.6 F g^{-1} at 3 A g^{-1}). Moreover, an assembled NS-3//AC ASC device exhibits an outstanding energy density of 38.5 W h kg^{-1} at a power density of 374.9 W kg^{-1} (22 W h kg^{-1} at 7615.4 W kg^{-1}), implying its great application potential in the next generation of high-performance supercapacitors.

Conflicts of interest

There are no conflicts to declare.

Acknowledgements

The work is thank to the financial support from the National Natural Science Foundation of China (No. 11504267, 11504269).

References

1 H. Chen, X. L. Liu and J. M. Zhang, Rational synthesis of hybrid $NiCo_2S_4$@MnO_2 heterostructures for supercapacitor electrodes, *Ceram. Int.*, 2016, **42**, 8099–8914.
2 J. R. Miller and P. Simon, Electrochemical capacitors for energy management, *Science*, 2008, **321**, 651–652.
3 M. Sun, X. Liu, G. D. Zhao, W. C. Kong, J. Y. Xuan, S. G. Tan, Y. P. Sun, S. Wei, J. F. Ren and G. C. Yin, Sn^{4+} doping combined with hydrogen treatment for CdS/TiO_2 photoelectrodes: an efficient strategy to improve quantum dots loading and charge transport for high photoelectrochemical performance, *J. Power Sources*, 2019, **430**, 80–89.
4 M. Sun, J. Tie, G. Cheng, T. Lin, S. Peng, F. Deng, F. Ye and L. Yu, In Situ Growth of Burl-like Nickel Cobalt Sulfide on Carbon Fiber as High-Performance Supercapacitors, *J. Mater. Chem. A*, 2015, **3**, 1730–1736.
5 Y. R. Zhu, Z. B. Wu and M. J. Jing, Mesoporous $NiCo_2S_4$ nanoparticles as high-performance electrode materials for supercapacitors, *J. Power Sources*, 2015, **273**, 584–590.
6 J. J. Yoo, K. Balakrishnan, J. Huang, V. Meunier, B. G. Sumpter, A. Srivastava, M. Conway, A. L. Reddy, J. Yu, R. Vajtai and P. M. Ajayan, Ultrathin planar graphene supercapacitors, *Nano Lett.*, 2011, **11**, 1423–1427.
7 G. Wang, L. Zhang and J. Zhang, A review of electrode materials for electrochemical supercapacitors, *Chem. Soc. Rev.*, 2012, **41**, 797–828.
8 X. L. Guo, G. Li, M. Kuang, L. Yu and Y. X. Zhang, Tailoring kirkendall effect of the KCu_7S_4 microwires towards CuO@MnO_2 core–shell nanostructures for supercapacitors, *Electrochim. Acta*, 2015, **174**, 87–92.
9 T. Zhai, L. M. Wan, S. Sun, Q. Chen, J. Sun, Q. Y. Xia and H. Xia, Phosphate ion functionalized Co_3O_4 ultrathin nanosheets with greatly improved surface reactivity for

high performance pseudocapacitors, *Adv. Mater.*, 2017, **29**, 1604167–1604174.

10 Z. F. Zeng, B. Q. Xiao, X. H. Zhu, J. G. Zhu, D. Q. Xiao and J. L. Zhu, Flower-like binary cobalt-nickel oxide with high performance for supercapacitor electrode via cathodic electrode position, *Ceram. Int.*, 2017, **43**, 633–638.

11 H. Jiang, P. S. Lee and C. Z. Li, 3D carbon based nanostructures for advanced supercapacitors, *Energy Environ. Sci.*, 2013, **6**, 41–53.

12 L. Huang, D. C. Chen and Y. Ding, Nickel–Cobalt Hydroxide Nanosheets Coated on $NiCo_2O_4$ Nanowires Grown on Carbon Fiber Paper for High-Performance Pseudocapacitors, *Nano Lett.*, 2013, **17**, 3135–3139.

13 J. W. Xiao, L. Wan and S. H. Yang, Design Hierarchical Electrodes with Highly Conductive $NiCo_2S_4$ Nanotube Arrays Grown on Carbon Fiber Paper for High Performance Pseudocapacitors, *Nano Lett.*, 2014, **14**, 831–838.

14 M. C. Liu, L. B. Kong, X.-J. Ma, C. Lu, X. M. Li, Y. C. Luo and L. Kang, Hydrothermal process for the fabrication of $CoMoO_4 \cdot 0.9H_2O$ nanorods with excellent electrochemical behavior, *New J. Chem.*, 2012, **36**, 1713–1718.

15 J. Jiang, Y. Li, J. Liu, X. Huang, C. Yuan and X. W. Lou, Recent advances in metal oxide-based electrode architecture design for electrochemical energy storage, *Adv. Mater.*, 2012, **24**, 5166–5180.

16 X. Xia, J. Tu, Y. Zhang, X. Wang, C. Gu, X. B. Zhao and H. J. Fan, High-quality metal oxide core/shell nanowire arrays on conductive substrates for electrochemical energy storage, *ACS Nano*, 2012, **6**, 5531–5538.

17 Y. Meng, P. Sun, W. He, B. Teng and X. Xu, Uniform P Doped Co–Ni–S Nanostructures for Asymmetric Supercapacitors with Ultra-high Energy Densities, *Nanoscale*, 2018, **11**, 688–697.

18 S. Tang, B. Zhu, X. Shi, J. Wu and X. Meng, Wearable High-Performance Supercapacitors Based on Silver-Sputtered Textiles with $FeCo_2S_4$–$NiCo_2S_4$ Composite Nanotube-Built Multitripod Architectures as Advanced Flexible Electrodes, *Adv. Energy Mater.*, 2017, **7**, 1601985.

19 X. Liu, R. Ma, Y. Bando and T. Sasaki, A general strategy to layered transition-metal hydroxide nanocones: tuning the composition for high electrochemical performance, *Adv. Mater.*, 2012, **24**, 2148–2153.

20 Y. Song, X. Cai, X. Xu and X. Liu, Integration of Nickel–Cobalt double hydroxide nanosheets and polypyrrole film with functionalized partial-exfoliated graphite for asymmetric supercapacitors with Improved Rate capability, *J. Mater. Chem.*, 2015, **3**, 14712–14720.

21 S. Kulvinder, k. Sushil and A. Kushagra, Three-dimensional Graphene with MoS_2 Nanohybrid as Potential Energy Storage/Transfer Device, *Sci. Rep.*, 2017, **25**, 9458–9470.

22 Y. P. zhou, J. Li, Y. Yang and B. Luo, Unique 3D flower-on-sheet nanostructure of NiCo-LDHs: Controllable microwave-assisted synthesis and its application for advanced supercapacitors, *J. Alloys Compd.*, 2019, **788**, 1029–1036.

23 Z. Cai, A. Wu, H. Yan, Y. Xiao, C. Chen, C. Tian, L. Wang, R. Wang and H. Fu, Hierarchical Whisker-on-sheet NiCoP with Adjustable Surface Structure for Efficient Hydrogen Evolution Reaction, *Nanoscale*, 2018, **10**, 7619–7629.

24 Y. H. Xiao, D. C. Su and X. Z. Wang, In suit growth of ultradispersed $NiCo_2S_4$ nanoparticles on graphene for asymmetric supercapacitors, *Electrochim. Acta*, 2015, **176**, 44–50.

25 J. Feng, X. Sun, C. Wu, L. Peng, C. Lin, S. Hu, J. Yang and Y. Xie, Metallic Few-Layered VS_2 Ultrathin Nanosheets: High Two-Dimensional Conductivity for In-Plane Supercapacitors, *J. Am. Chem. Soc.*, 2011, **133**, 17832–17838.

26 L. Shen, L. Yu, H. B. Wu, X.-Y. Yu, X. Zhang and X. W. D. Lou, Formation of nickel cobalt sulfide ball-in-ball hollow spheres with enhanced electrochemical pseudocapacitive properties, *Nat. Commun.*, 2015, **6**, 6694.

27 J. Xiao, L. Wan, S. Yang, F. Xiao and S. Wang, Design hierarchical electrodes with highly conductive $NiCo_2S_4$ nanotube arrays grown on carbon fiber paper for high-performance pseudocapacitors, *Nano Lett.*, 2014, **14**, 831–838.

28 H. Chen, J. Jiang, L. Zhang, H. Wan, T. Qi and D. Xia, Highly conductive $NiCo_2S_4$ urchin-like nanostructures for high-rate pseudocapacitors, *Nanoscale*, 2013, **5**, 8879–8883.

29 A. R. John and J.-H. Park, Rambutan-like cobalt nickel sulfide ($CoNi_2S_4$) hierarchitecture for high-performance symmetric aqueous supercapacitors, *J. Ind. Eng. Chem.*, 2018, **63**, 73–83.

30 F. L. Zhao, W. X. Huang and H. T. Zhang, Facile synthesis of $CoNi_2S_4/Co_9S_8$ composites as advanced electrode materials for supercapacitors, *Appl. Surf. Sci.*, 2017, **426**, 1206–1212.

31 L. G. Beka, X. Li and W. H. Liu, Nickel Cobalt Sulfide core/shell structure on 3D Graphene for supercapacitor application, *Sci. Rep.*, 2017, **18**, 2105–2116.

32 D. P. Cai, D. D. Wang and C. X. Wang, Construction of desirable $NiCo_2S_4$ nanotube arrays on nickel foam substrate for pseudocapacitors with enhanced performance, *Electrochim. Acta*, 2015, **151**, 35–41.

33 Y. H. Li, L. J. Cao and L. Qiao, Ni–Co sulfide nanowires on nickel foam with ultrahigh capacitance for asymmetric supercapacitors, *J. Mater. Chem. A*, 2014, **2**, 6540–6548.

34 X. H. Xiong, G. Waller and D. Ding, Controlled synthesis of $NiCo_2S_4$ nanostructured arrays on carbon fiber paper for high-performance pseudocapacitors, *Nano Energy*, 2015, **16**, 71–80.

35 J. Liao, P. Zou, S. Su, A. Nairan, Y. Wang, D. Wu, C. P. Wong, F. Kang and C. Yang, Hierarchical nickel nanowire@$NiCo_2S_4$ nanowhiskers composite arrays with test-tube-brush-like structure for high-performance supercapacitors, *J. Mater. Chem. A*, 2018, **6**, 15284–15293.

36 Y. Wen, S. Peng, Z. Wang, J. Hao, T. Qin, S. Lu, J. Zhang, D. He, X. Fan and G. Cao, Facile Synthesis of Ultrathin $NiCo_2S_4$ Nano-petals Inspired by Blooming Buds for High-Performance Supercapacitors, *J. Mater. Chem. A*, 2017, **5**, 7144–7152.

37 Y. Xu, L. Wang, X. Liu, S. Zhang, C. Liu, D. Yan, Y. Zeng, Y. Pei, Y. Liu and S. Luo, Monolayer MoS_2 with S Vacancy from Interlayer Spacing Expanded Counterparts for Highly

Efficient Electrochemical Hydrogen Production, *J. Mater. Chem. A*, 2016, **4**, 16524–16530.

38 X. Y. Wu, X. P. Han, X. Y. Ma, W. Zhang, Y. D. Deng, C. Zhong and W. B. Hu, Morphology-Controllable Synthesis of Zn–Co-Mixed Sulfide Nanostructures on Carbon Fiber Paper Toward Efficient Rechargeable Zinc–Air Batteries and Water Electrolysis, *ACS Appl. Mater. Interfaces*, 2017, **9**, 12574–12583.

39 J. Jiang, J. P. Liu, X. T. Huang and Y. Y. Li, General Synthesis of Large-Scale Arrays of One-Dimensional Nanostructured Co_3O_4 Directly on Heterogeneous Substrates, *Cryst. Growth Des.*, 2010, **10**, 70–75.

40 X. J. Chen, D. Chen and X. Y. Guo, Facile Growth of Caterpillar-like $NiCo_2S_4$ Nanocrystal Arrays on Nickle Foam for High-Performance Supercapacitors, *ACS Appl. Mater. Interfaces*, 2017, **9**, 18774–18781.

41 L. Lin, J. Liu, T. Liu, J. Hao, K. Ji, R. Sun, W. Zeng and Z. Wang, Growth-Controlled $NiCo_2S_4$ Nanosheet Arrays with Self-Decorated Nanoneedles for High-Performance Pseudocapacitors, *J. Mater. Chem. A*, 2015, **3**, 17652–17658.

42 S. C. Tang, B. G. Zhu, X. L. Shi and J. Xu, General controlled sulfidation toward achieving novel nanosheet-built porous square-$FeCo_2S_4$-tube arrays for high-performance asymmetric all-solid-state pseudocapacitors, *Adv. Energy Mater.*, 2017, **7**, 1601985.

43 V. Augustyn, P. Simonbc and B. Dunn, Pseudocapacitive oxide materials for high rate electrochemical energy storage, *Energy Environ. Sci.*, 2014, **7**, 1597–1614.

44 D. Cai, D. Wang, C. Wang, B. Liu, L. Wang, Y. Liu, Q. Li and T. Wang, Construction of desirable $NiCo_2S_4$ nanotube arrays on nickel foam substrate for pseudocapacitors with enhanced performance, *Electrochim. Acta*, 2015, **151**, 35–41.

45 Z. H. Xu, S. S. Sun and W. Cui, Interconnected network of ultrafine MnO_2 nanowires on carbon cloth with weed-like morphology for high-performance supercapacitor electrodes, *Electrochim. Acta*, 2018, **268**, 340–346.

46 Q. Zong, H. Yang and Q. L. Zhang, Three-dimensional coral-like NiCoP@C@$Ni(OH)_2$ core–shell nanoarrays as battery-type electrodes to enhance cycle stability and energy density for hybrid supercapacitors, *Chem. Eng. J.*, 2019, **361**, 1–11.

47 Q. Zong, H. Yang and Q. L. Zhang, $NiCo_2O_4$/NiCoP nanoflake-nanowire arrays: a homogeneous hetero-structure for high performance asymmetric hybrid supercapacitors, *Dalton Trans.*, 2018, **47**, 16320–16328.

48 H. N. Jia, Z. Y. Wang and X. H. Zheng, Interlaced Ni–Co LDH nanosheets wrapped Co_9S_8 nanotube with hierarchical structure toward high performance supercapacitors, *Chem. Eng. J.*, 2018, **351**, 348–355.

49 H. N. Jia, Z. Y. Wang, C. Li and X. H. Zheng, Designing oxygen bonding between reduced graphene oxide and multishelled Mn_3O_4 hollow spheres for enhanced performance of supercapacitors, *J. Mater. Chem. A*, 2019, **7**, 6686–6694.

50 N. Wang, B. L. Sun, P. Zhao and W. C. Hu, Electrodeposition preparation of $NiCo_2O_4$ mesoporous film on ultrafine nickel wire for flexible asymmetric supercapacitors, *Chem. Eng. J.*, 2018, **345**, 31–38.

51 M. D. Stoller and R. S. Ruoff, Best practice methods for determining an electrode material's performance for ultracapacitors, *Energy Environ. Sci.*, 2010, **3**, 1294–1301.

